AIAA JOURNAL
Vol. 47, No. 8, August 2009

Hermite-Based Mesh Adaptation for Functional Outputs Improvement in Fluid Flow Simulation

Lakhdar Remaki* and Wagdi G. Habashi†
McGill University, Montreal, Quebec H3A 2S6, Canada

DOI: 10.2514/1.33437

The objective of this work is to focus the mesh adaptation process in computational fluid dynamics codes to better estimate the drag, lift, and moment coefficients. This is achieved by an integral-based error indicator that controls the element size and the classical Hessian-based error to control the element orientation. Using such an error indicator leads to the improvement of the physical quantities formulated by integrals, such as the aforementioned drag, lift, and moment coefficients. In addition, it avoids the excessive variation in element size that occurs when a pure Hessian is used. As a consequence, the entire field solution accuracy is improved.

Nomenclature

C_d	=	drag coefficient
C_l	=	lift coefficient
C^1	=	space of continuous functions with continuous first derivatives
H	=	Hessian matrix
H^1	=	Sobolev functional space
IR^3	=	three-dimensional space of real numbers
$P_k(\Omega)$	=	space of polynomials of order k
$\delta_{i,j}$	=	Kronecker symbol
Ω	=	open set of IR^3

I. Introduction

COMPUTATIONAL fluid dynamics accuracy is the subject of much debate and research within the fluid flow simulation community. One of the most direct ways of improving accuracy, without lengthy mesh effect studies, is to use mesh optimization. Such automatic mesh adaptation techniques are being developed to improve the convergence and accuracy and to permit simulations starting from a reasonably coarse initial grid. A robust and efficient three-dimensional automatic mesh adaptation methodology, with CAD integrity, has been developed [1–5]. The adaptation procedure uses an a posteriori interpolation error estimate, for which the magnitude and direction are controlled by the matrix of local second derivatives of a selected flow variable. This error is projected over the mesh edges and drives the nodal movement algorithm, as well as the edge refinement, coarsening, and face swapping strategies.

However, this adaptation process generally results in highly stretched and large elements connected to smaller ones. This, although highly cost effective in terms of accuracy of variables, may lead to a loss of accuracy for functional outputs (global integrals) such as the drag, lift, or moment coefficients. In addition, although finite element approaches have no problem handling stretched or skewed grids, finite volume methods are much more sensitive to such stretching. However, both methods are sensitive to the sudden growth of element size. Therefore, it is important to control the jump in the anisotropy of elements to make the approach suitable to a larger range of solvers. In other words, it would be better to control the error integral of output scalars rather than controlling second derivatives, which end up being responsible for the excessive variation of element size when varying drastically near discontinuities. Note that we are talking here about the numerical approximation of the derivatives, for which theoretical value is infinite at discontinuities.

In general, an adjoint-based method is used for that purpose. Via the linear adjoint problem, the error indicator is connected to the local residual error of the primary solution. Details of the formulation of such methods can be found in [6–8], and important extensions are proposed in [9–12].

To improve the accuracy of predicting functional outputs, we propose here an error indicator based on Hermitian interpolation. This error is used to control the element size and is then incorporated within the Hessian-based metric for anisotropic adaptation. We propose a way to control the stretching, which is applicable to any kind of error formulated by a metric, including the pure Hessian-based error. The drastic volume size variation is controlled as integrals vary smoothly from regions with high curvature to regions of low curvature, which is not the case with the Hessian, especially in the vicinity of discontinuities. We show that the Hermite-based approach provides good results, is easy to implement, and is faster than an adjoint-based method as there is no need to solve/invert a global matrix.

To stabilize the particular finite element method (FEM) solver used in the present simulations, the isovalue-oriented diffusion (ISOD) [13] artificial viscosity is considered, with a slight modification. To demonstrate the efficiency of the proposed Hermite-based adaptation approach, two viscous flow test cases are performed.

In Secs. II and III, general overviews of the ISOD artificial viscosity and of the Hessian-based mesh optimization methodology are given. In Secs. IV and V, the proposed Hermite-based functional outputs adaptation is developed for both isotropic and anisotropic grids. Test cases are performed and shown in Sec. VI, and conclusions are drawn in Sec. VII.

II. Isovalue-Oriented Diffusion Stabilized Finite Element Method

The linear finite element solver FENSAP is used for all test cases. This FEM code is stabilized using the artificial viscosity ISOD first introduced in [13]. This artificial viscosity better captures discontinuities and avoids the hard task of estimating optimal viscosity coefficients required by other approaches. The idea is to diffuse along solution isovalues that are parallel to discontinuities, permitting their stabilization without smearing. The method is explained as follows.

Presented as Paper 1297 at the The 45th AIAA Aerospace Science Meeting, Reno, NV, 8–11 January 2007; received 13 July 2007; revision received 11 December 2008; accepted for publication 19 December 2008.

*Research Associate, Computational Fluid Dynamics Laboratory, 688 Sherbrooke Street West, 7th Floor; currently Research Officer, University of Wales Swansea, Swansea, Wales SA2 8PP, United Kingdom.

†Professor, NSERC-J. Armand Bombardier Industrial Research Chair for Multidisciplinary Computational Fluid Dynamics, and Director, Computational Fluid Dynamics Laboratory; wagdi.habashi@mcgill.ca. Associate Fellow AIAA.

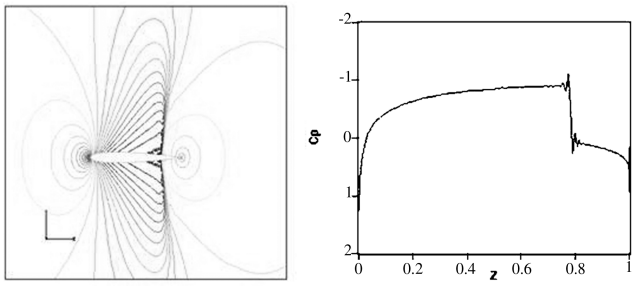

a) The initial data: noisy euler solution around NACA 0012, the mach profile

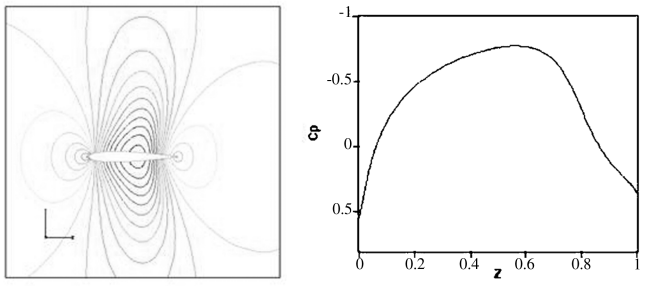

b) Diffusion solution for CU method

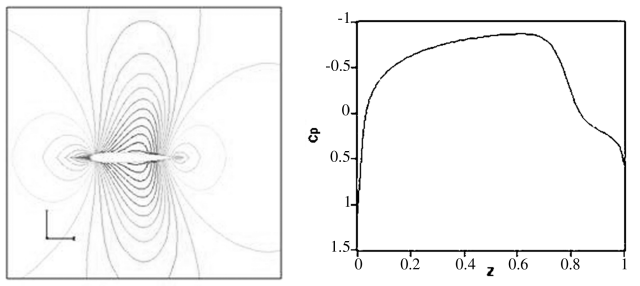

c) Diffusion solution for SU method

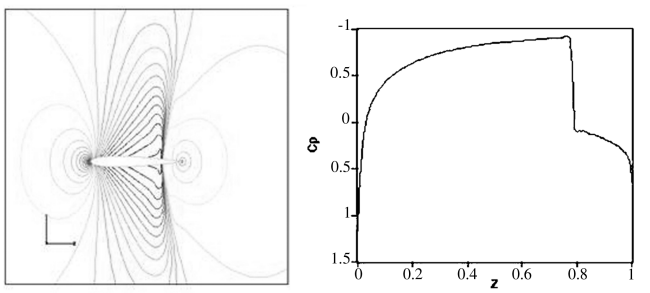

d) Diffusion solution for ISOD method

Fig. 1 NACA 0012 wing: comparison of the diffusion effect around discontinuities between the classical upwind, SU, and ISOD methods.

Let Q be a C^1 given scalar function defined on an open set Ω of IR^3. The isovalues oriented diffusion operator $\Delta_{\text{isod}}Q$ is defined as the diffusion operator in the plane orthogonal to the gradient of Q, that is,

$$\Delta_{\text{isod}}Q = \Delta_{\underset{\eta_1}{\rightarrow}}Q + \Delta_{\underset{\eta_2}{\rightarrow}}Q \tag{1}$$

where $(\nabla Q, \boldsymbol{\eta}_1, \boldsymbol{\eta}_2)$ forms a normalized orthogonal reference system on each point of Ω. The analytical expression of $\Delta_{\text{isod}}Q$ (see [6] for details) is given by

$$\Delta_{\text{isod}} = \sum_{i,j=1}^{3} (\delta_{i,j} - \lambda_{i,j}(Q))\partial_{x_i}\partial_{x_j}Q \tag{2}$$

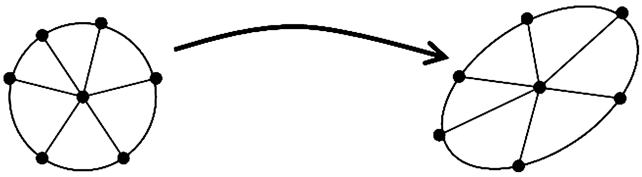

Fig. 2 Hessian metric transformation from a sphere to an ellipsoid.

where $\lambda_{i,j}(Q) = \frac{(2-\delta_{i,j})(\partial_{x_i}Q)(\partial_{x_j}Q)}{(\partial_{x_1}Q)^2+(\partial_{x_2}Q)^2+(\partial_{x_3}Q)^2}$, and $\delta_{i,j}$ is the Kronecker symbol.

Let the Navier–Stokes equations in conservative form be

$$\partial_t U + \nabla.F(U) - \nabla.G(U, \nabla U) = S \tag{3}$$

where S is a source term,

$$U = \begin{bmatrix} \rho \\ \rho u \\ \rho v \\ \rho w \\ E \end{bmatrix}$$

$$F = (F_1, F_2, F_3) \quad \text{with } F_1 = \begin{bmatrix} \rho u \\ \rho u^2 + P \\ \rho uv \\ \rho uw \\ (E+P)u \end{bmatrix}$$

$$F_2 = \begin{bmatrix} \rho v \\ \rho uv \\ \rho v^2 + P \\ \rho vw \\ (E+P)v \end{bmatrix}, \qquad F_2 = \begin{bmatrix} \rho w \\ \rho uw \\ \rho vw \\ \rho w^2 + P \\ (E+P)w \end{bmatrix}$$

$$G = (G_1, G_2, G_3) \quad \text{with } G_i = \begin{bmatrix} 0 \\ \tau_{i1} \\ \tau_{i2} \\ \tau_{i3} \\ \tau_{1i}u + \tau_{2i}v + \tau_{3i}w + k\partial_{x_i}\Theta \end{bmatrix}$$

$$i = 1, 3$$

where (u, v, w) are the components of the velocity, ρ is the density, P is the pressure, E is the total energy, τ_{ji} are the components of the viscous part of the stress tensor, Θ is the absolute temperature, and $k$is the heat conductivity.

Consider these equations, with the ISOD artificial viscosity term:

$$\partial_t U + \nabla.F(U) - \nabla.G(U, \nabla U) - \varepsilon\Delta_{\text{ISOD}}U = S \tag{4}$$

where ε is a scalar viscosity coefficient that tends to zero. To obtain a weak formulation of the ISOD operator for linear FEM, we considered in [13] diffusion along the perpendicular plane to an average value of the reconstructed gradient computed at the center of the element. The transmission terms between cells are neglected; then the diffusion operator $-\varepsilon\Delta_{\text{ISOD}}U$ can be put in the form $-\varepsilon\nabla B\nabla U$ and the weak form is derived. In more detail, let us consider the classical finite element discretization of the Navier–Stokes equations. Let ϑ_h be the trial solution space:

Table 1 RAE 2822 wing test case reference data

Mach number	0.73
Reynolds number	6.5×10^6
Angle of attack, deg	2.79
Freestream static pressure, Pa	101325
Freestream static temperature, K	288
Characteristic length, m	0.3809
Reference area, m^2	0.0171
Span. m	0.045

Table 2 RAE 2822 wing test case experimental data and CFD comparisons

	Test results [21]	Solution with AFO	Solution with IFO	Solution with HBA	Other CFD [17]
Lift C_L	0.8030	0.7972	0.7961	0.7386	0.8415
Drag C_D	0.0168	0.0169	0.0169	0.0178	0.0181

$$\vartheta_h = \{v/v(.,t) \in H^1(\Omega)^m, t \in [0,T], v/\Omega_e \in P_k(\Omega^e)^m, v(.,t) = g \quad \text{on } \Gamma_g\}$$

and ω_h the weighting function space (note that, in our case, $k = 1$):

$$W_h = \{w/w(.,t) \in H^1(\Omega)^m, t \in [0,T], v/\Omega_e \in P_k(\Omega^e)^m, w(.,t) = 0 \quad \text{on } \Gamma_g\}$$

The weak formulation of Eq. (4) is then given by finding

$$B_g^\varepsilon = \varepsilon(I - A_g) \tag{5}$$

$$A_g(V) = \begin{pmatrix} \lambda_{1,1}(V) & \lambda_{1,2}(V) & \lambda_{1,3}(V) \\ \lambda_{2,1}(V) & \lambda_{2,2}(V) & \lambda_{2,3}(V) \\ \lambda_{3,1}(V) & \lambda_{3,2}(V) & \lambda_{3,3}(V) \end{pmatrix} \tag{6}$$

where the subscript g refers to the global reconstructed derivatives versus local derivatives. In this work, we observe that by considering the interpolated value of the reconstructed gradients at each Gauss

$$V \in \vartheta_h \underbrace{\int_\Omega (W.V_t - \nabla W.F(V) + \nabla W.G(V,\nabla V) + W.S)\,\mathrm{d}\Omega - \int_\Gamma W(-F(V) + G(V,\nabla V).\mathbf{n}\,\mathrm{d}\Gamma}_{\text{Navier–Stokes term}}$$
$$+ \underbrace{\sum_e \int_{\Omega^e} \nabla W.(B^\varepsilon \nabla V)\,\mathrm{d}\Omega - \int_{\partial\Omega^e \cap \Gamma} W(B^\varepsilon V).\mathbf{n}\,\mathrm{d}\Gamma}_{\text{ISOD viscosity term}} = 0 \quad \forall\ W \in \omega_h$$

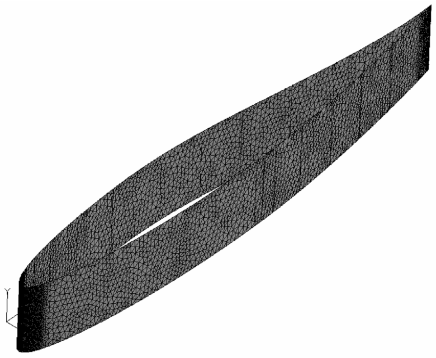

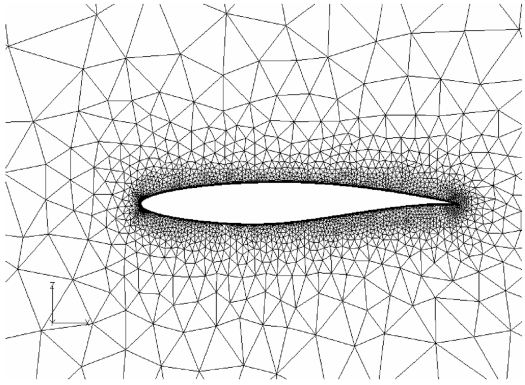

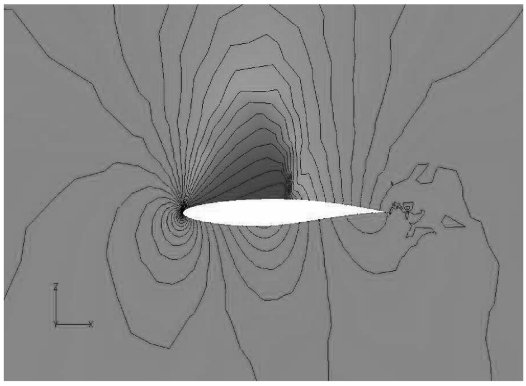

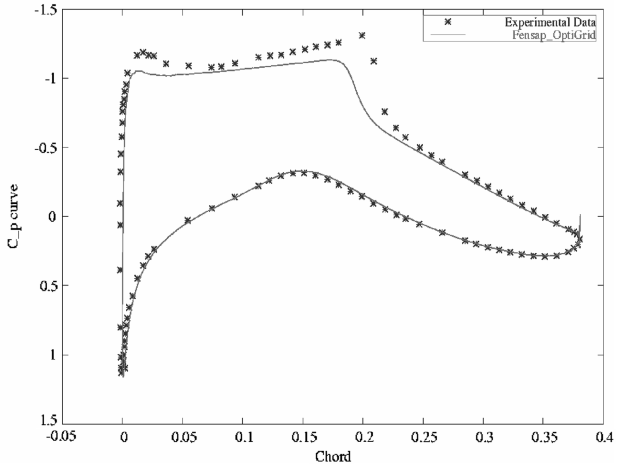

Fig. 3 RAE 2822 wing: Cp profile on the initial grid.

point, rather than considering the average over the element as in [13], ISOD becomes more robust.

To demonstrate ISOD, Fig. 1 shows a noisy Euler solution on a NACA 0012 at Mach = 0.85 and a 0 deg angle of attack. This solution is considered as the initial condition of a purely diffusive equation using, in turn, the classical Laplacian operator, the streamline upwinding (SU) operator, and, finally, the proposed ISOD operator. With the same amount of viscosity and after 10 time iterations, the figures show that the Laplacian and SU methods are highly diffusive (with less diffusion for the SU), removing the noise but considerably smearing the shock. The ISOD method shows a greater ability to remove noise and a higher quality of shock. For more details about the method, see [13].

III. Hessian-Based Mesh Adaptation

The mesh adaptation operations include node movement, edge refinement, coarsening, and swapping for hybrid grids consisting of any combination of tetrahedra, prisms, hexahedra, or pyramids. At all times during adaptation, the methodology respects the original CAD definition by reprojecting all surface points moved or created by adaptation onto the CAD.

The solution-based adaptation is driven by an a posteriori error estimate based on the Hessian of a selected scalar flow variable, because, for FEM/finite volume method solvers with linear basis functions, the truncation error is dominated by the second derivatives. When H is positive definite, it defines a metric; therefore, the error along a given vector could be interpreted as the length of the vector measured by the Hessian metric. Consequently, a metric T is derived from the Hessian by considering its absolute value $T = |H| = R^t|\Lambda|R$, where R is the eigenvector matrix of H and $|\Lambda| = \text{diag}\{|\lambda_1|, |\lambda_2|, |\lambda_3|\}$ is the matrix composed of the absolute values of the eigenvalues of H. The eigenvectors of T provide the local direction of the stretching, whereas the eigenvalues give its local magnitude, thus gradually creating anisotropy. The goal of the adaptation is to equidistribute the error (err) on the adapted grid, where the error along an edge in the Riemannian metric is computed as

$$\text{err} = \int_0^1 \sqrt{\mathbf{x}^T T(s)\mathbf{x}}\, \mathrm{d}s$$

where $\mathbf{x}$ is the vector that defines the edge.

The optimization algorithm uses several modification operations to set the error equal to a target value assigned in general by the user. In our approach and for all test cases, this is automatically determined

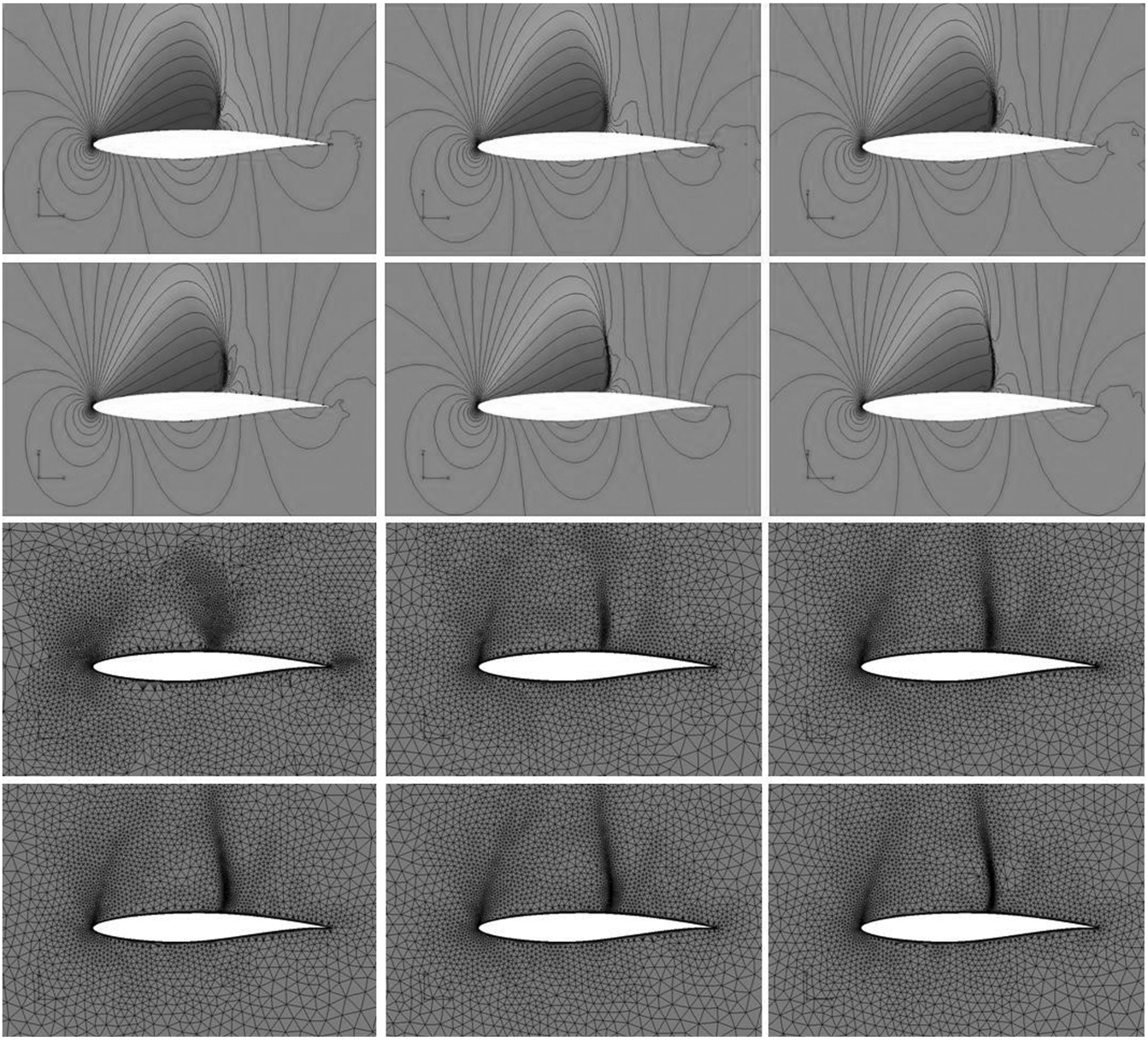

Fig. 4 RAE 2822 wing: Cp profiles and adapted grids using IFO adaptation.

using Otsu's threshold, as in [14]. The sequence of operations begins with node movement, edge refinement, and edge swapping on solid boundaries to satisfy a minimum and maximum edge length constraint, as well as a curvature constraint, yielding substantial surface CAD improvements. The process then continues with node movement in the entire domain, followed by refinement and coarsening, then swapping, before concluding with additional node movement. The method preserves CAD integrity by reprojecting boundary points onto the original surfaces during the adaptation process.

This technology has been widely tested in CFD applications and its efficiency demonstrated over a considerable set of test cases. However, the method shows some limitations in efficiently predicting global integral values such as drag, lift, or moment coefficients.

IV. Functional-Output-Based Mesh Adaptation

Drag, lift, and moments could be viewed as functional outputs. To improve functional output accuracy, it is necessary to estimate an integral error and use it as an error indicator. The most popular method to estimate this error is the adjoint-based method [5]. Via the linear adjoint problem, the indicator error is connected to the local residual error of the primary solution. Details of the formulation of the method can be found in [6–12]. This method requires the formulation of the discrete adjoint problem and then the solution of the resulting linear system. As an alternative, we propose to estimate the integral error by using a Hermitian interpolation to avoid inverting matrices. This method could be seen also as a characteristic-based method, because only the features of the scalar solution are used and no connection with the residual or other solver indictor is established.

Let us now describe the method. Recall that the goal is to minimize the integral error of a given quantity. Let

$$I = \int_{\Omega} u \, \mathrm{d}x$$

be the integral quantity (the functional output) we want to estimate; this could be the drag or lift coefficients, and

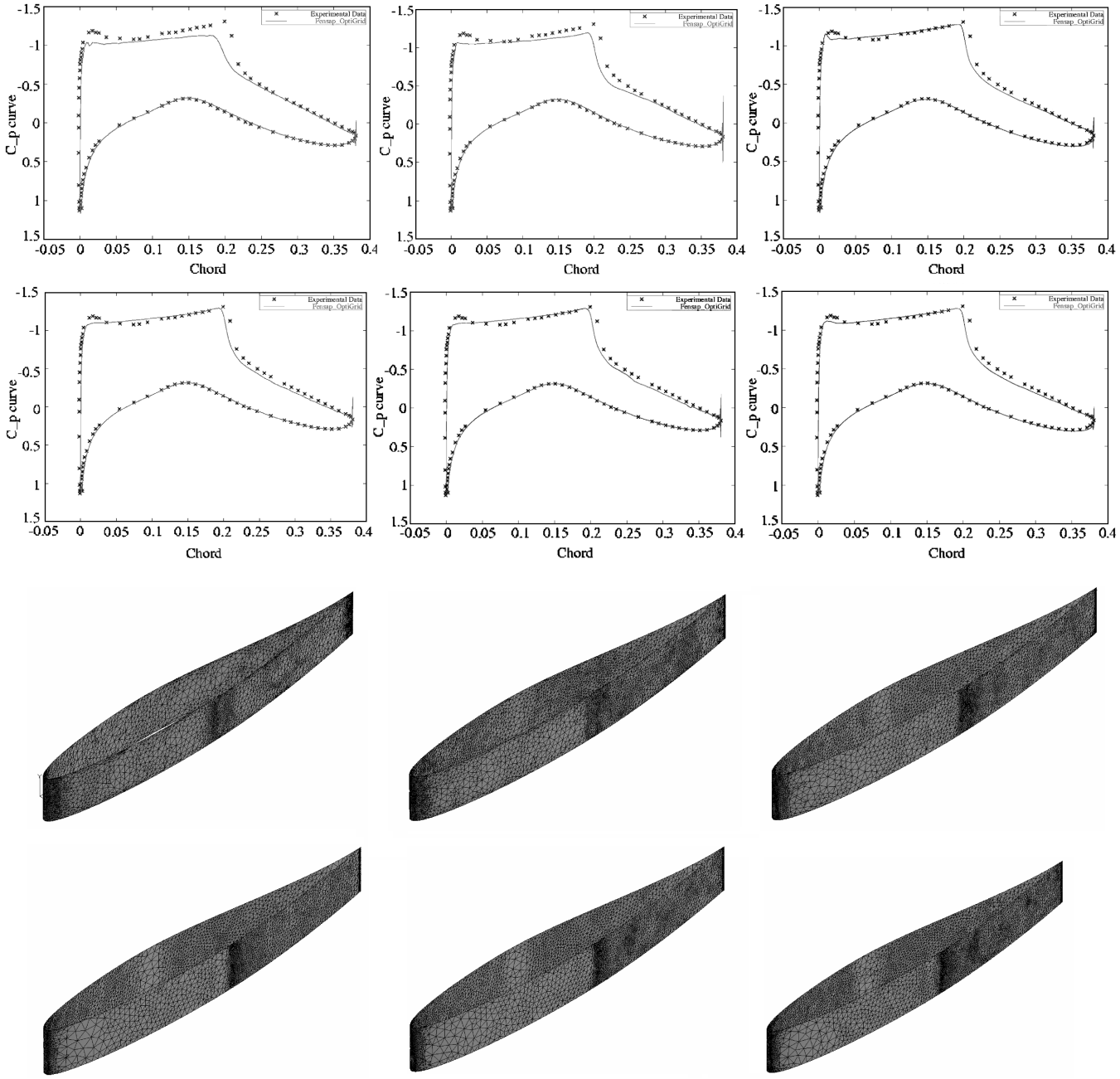

Fig. 5 RAE 2822 wing: Cp chordwise profiles and adapted grids using IFO adaptation.

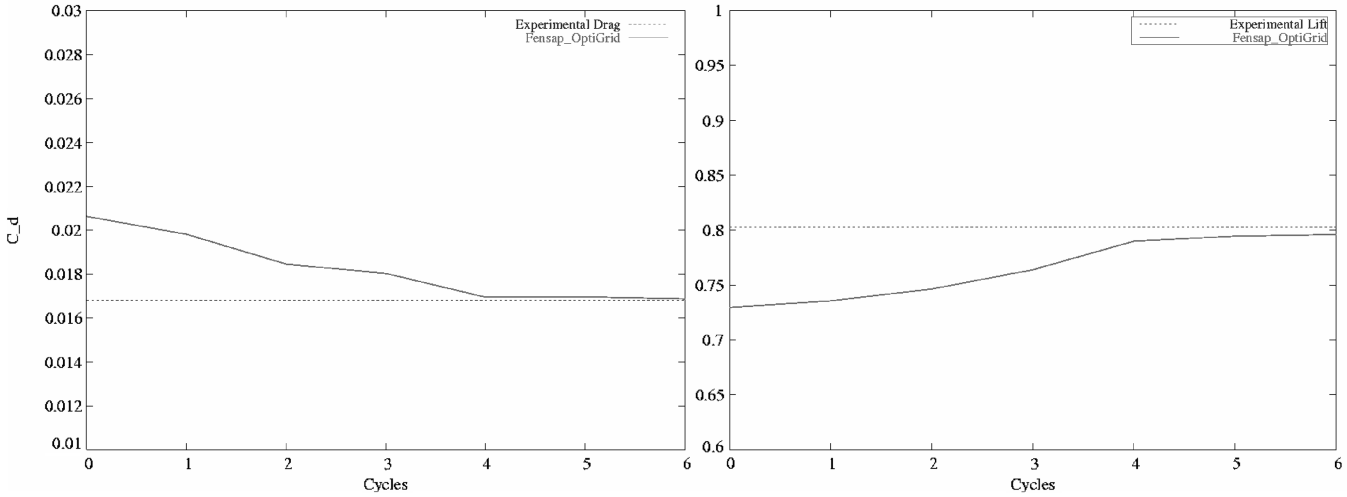

Fig. 6 RAE 2822 wing: drag and lift evolution with adaptation cycles (IFO).

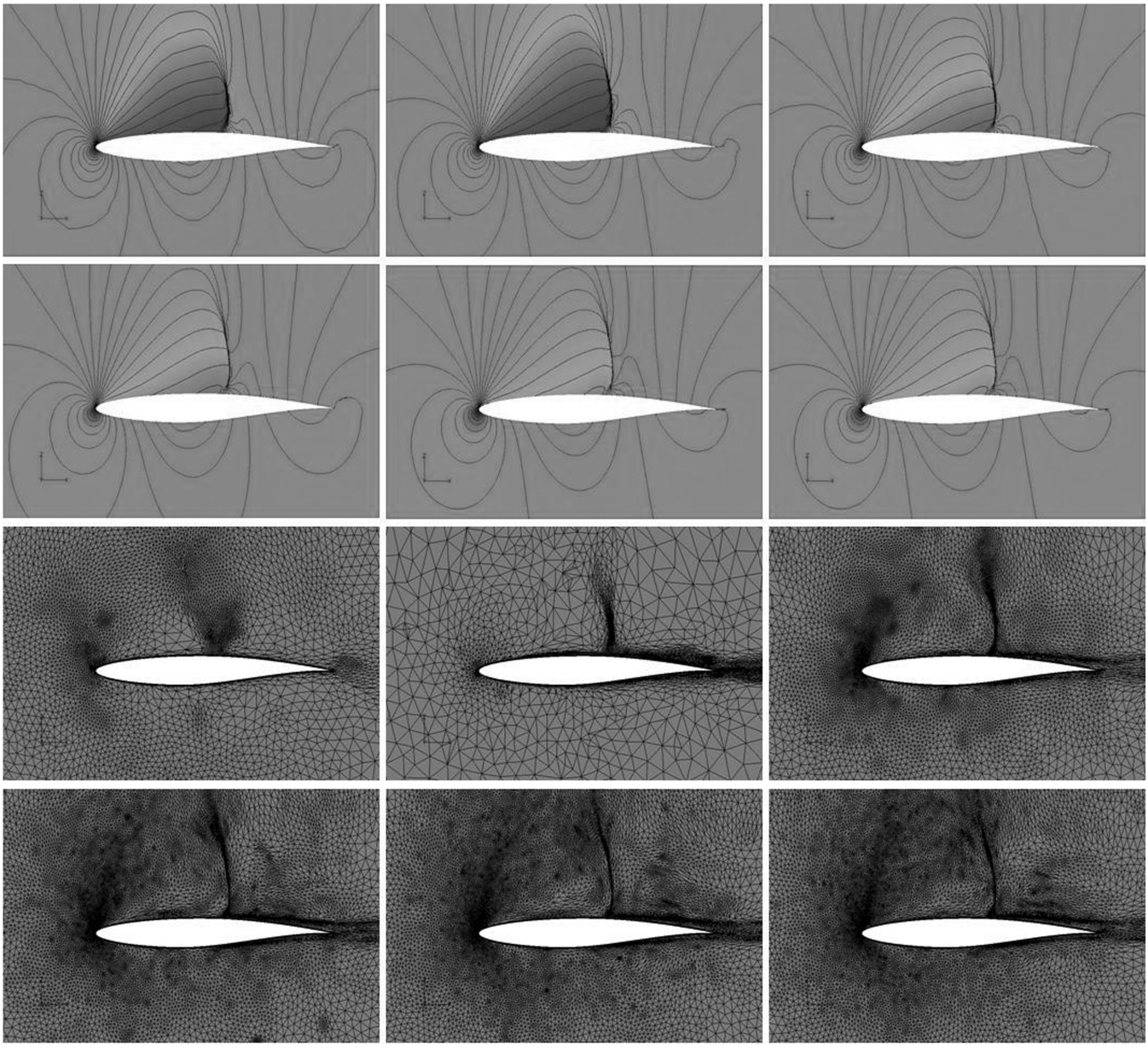

Fig. 7 RAE 2822 wing: Cp profiles and adapted grids using AFO adaptation.

$$I_h = \int_\Omega u_h \, \mathrm{d}x$$

is the estimated value, where u_h is the computed scalar. Let $E_h = |I - I_h|$ be the error. It is a well known claim that, in the case of Hessian-based mesh adaptation methodology, minimizing the error E_h over the domain could be achieved by equidistributing the error over edges. We will also adopt this procedure for our approach. Let $e_{i,j}$ be the edge connecting nodes i and j; then the error along the edge is given by

$$E_{e_{i,j}} = \left| \int_{e_{i,j}} u \, \mathrm{d}s - \int_{e_{i,j}} u_h \, \mathrm{d}s \right|$$

At each node, the values of the scalar u_h and the first derivatives $u'_h(i) = (1/\|e_{i,j}\|)\nabla u_h(i) \cdot e_{i,j}$ are available, $u'_h(j) = (1/\|e_{i,j}\|)\nabla u_h(j) \cdot e_{i,j}$, where $\nabla u_h(.)$, is the reconstructed gradient. This allows us to perform the Hermitian interpolation, which is a third-order polynomial, along the edge $e_{i,j}$ of the computed scalar. We refer to it by $u^H_{e_{i,j}}$. Then we propose to estimate the integral error along the edge $e_{i,j}$ by

$$E_{e_{i,j}} \approx \left| \int_{e_{i,j}} u_h \, \mathrm{d}s - \int_{e_{i,j}} u^H_{e_{i,j}} \, \mathrm{d}s \right| \tag{7}$$

Note that u_h is the linear interpolation of the computed solution.

For the adaptation process, an error E_i is defined at each node i by taking the average of the connected edges errors defined by Eq. (7). The node error just defined, which is a scalar, is multiplied by the identity matrix to obtain a metric, and then the Hessian metric is replaced by this new metric in the adaptation process. This leads naturally to an isotropic adaptation.

V. Anisotropic Functional-Output-Based Mesh Adaptation

Following some of the ideas of Venditti and Darmofal [9], implemented for two-dimensional triangular elements, the integral-error indicator derived earlier is incorporated within the Hessian metric. Consequently, the volume of the element (error over the

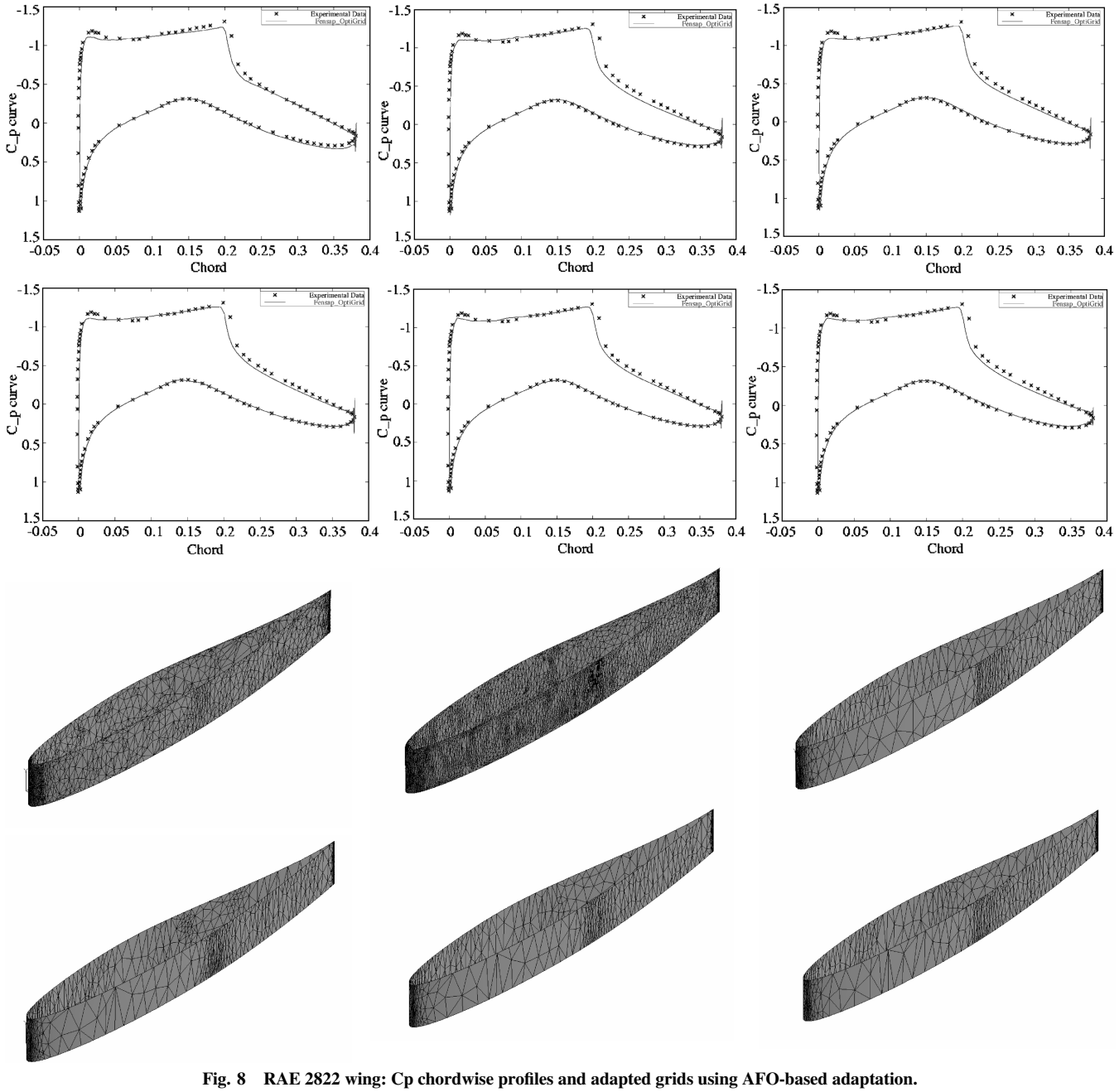

Fig. 8 RAE 2822 wing: Cp chordwise profiles and adapted grids using AFO-based adaptation.

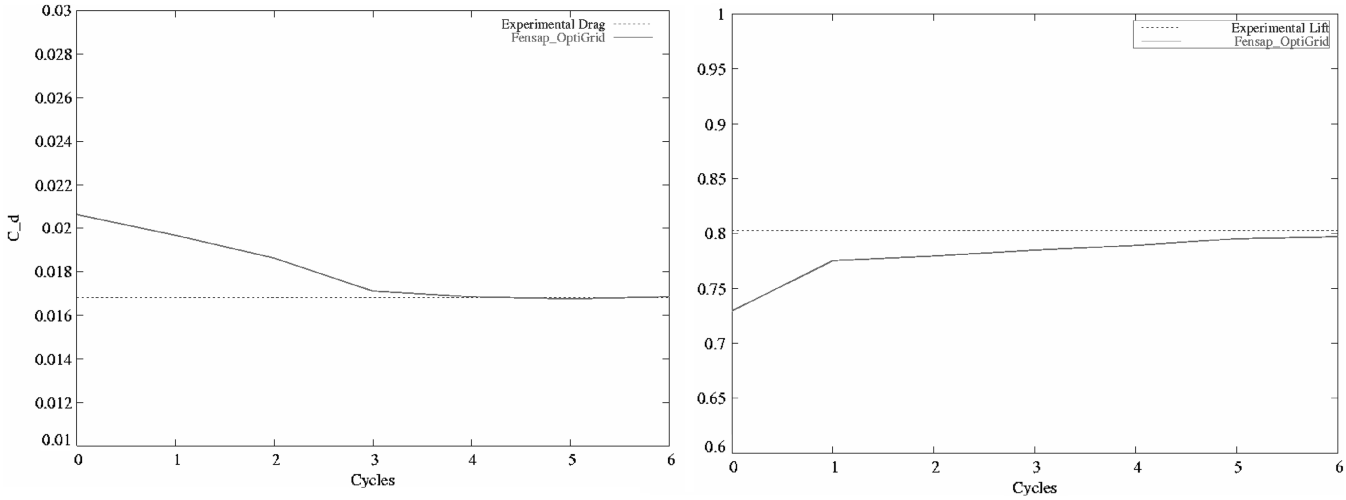

Fig. 9 RAE 2822 wing: drag and lift evolution with adaptation cycles (AFO).

element) is controlled by the functional output error, whereas the orientation and the stretching of the element are controlled by the Hessian. We generalize this approach first to three dimensions and then to any element topology. By equidistributing the error, we solve the equation $\langle MX, X\rangle = 1$, where M is the normalized (by the target error) Hessian metric; this transforms [2,15] a set of points into an ellipsoid (Fig. 2).

Now decompose M into its singular values, namely, $M = RDR^t$, where $D = \{\lambda_1, \lambda_1, \lambda_1\}$ is a diagonal matrix and R is a rotation matrix. Then we have

$$\langle MX, X\rangle = \langle RDR^tX, X\rangle = \langle DR^tX, R^tX\rangle$$

In the rotated reference frame, the ellipsoid equation is given by

$$\frac{y_1^2}{(\frac{1}{\sqrt{\lambda_1}})^2} + \frac{y_2^2}{(\frac{1}{\sqrt{\lambda_2}})^2} + \frac{y_3^2}{(\frac{1}{\sqrt{\lambda_3}})^2} = 1$$

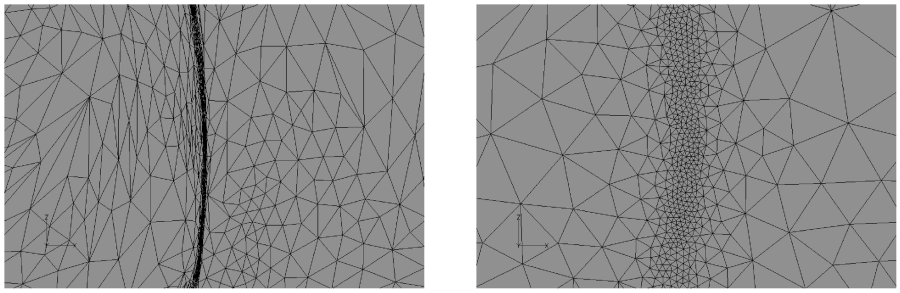

Fig. 10 RAE 2822 wing: anisotropic and isotropic adapted mesh around a shock (AFO/IFO).

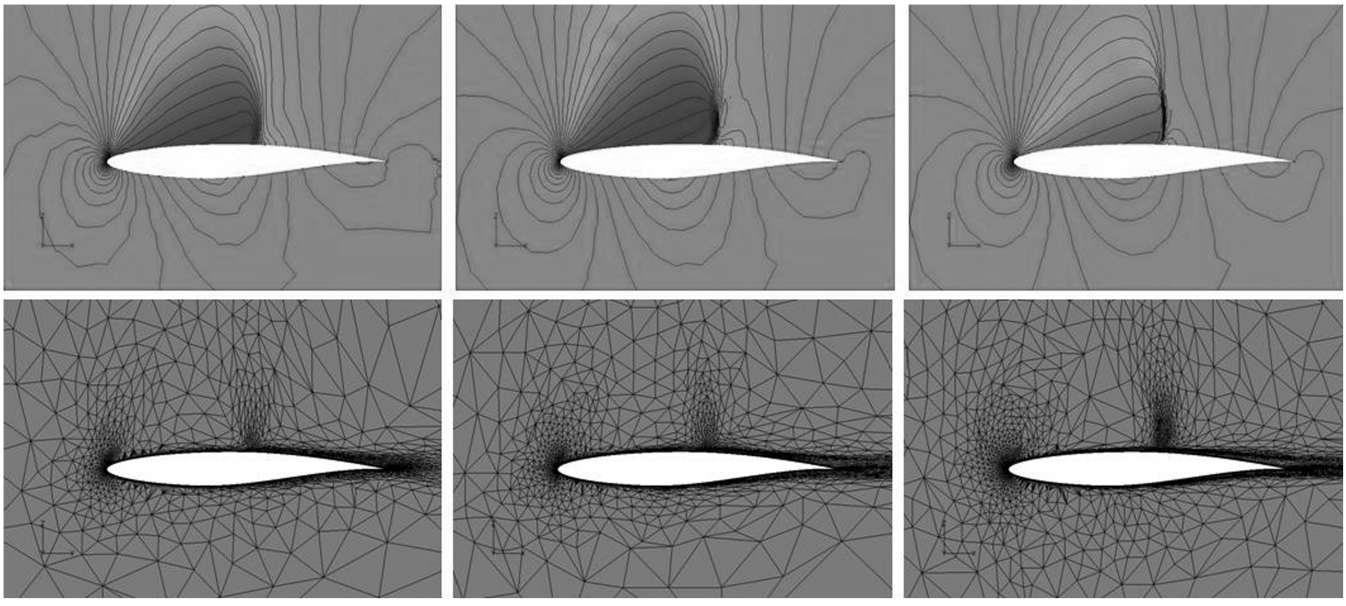

Fig. 11 RAE 2822 wing: Cp profiles and adapted grids using HBA. Only cycles 2, 4, and 6 are illustrated.

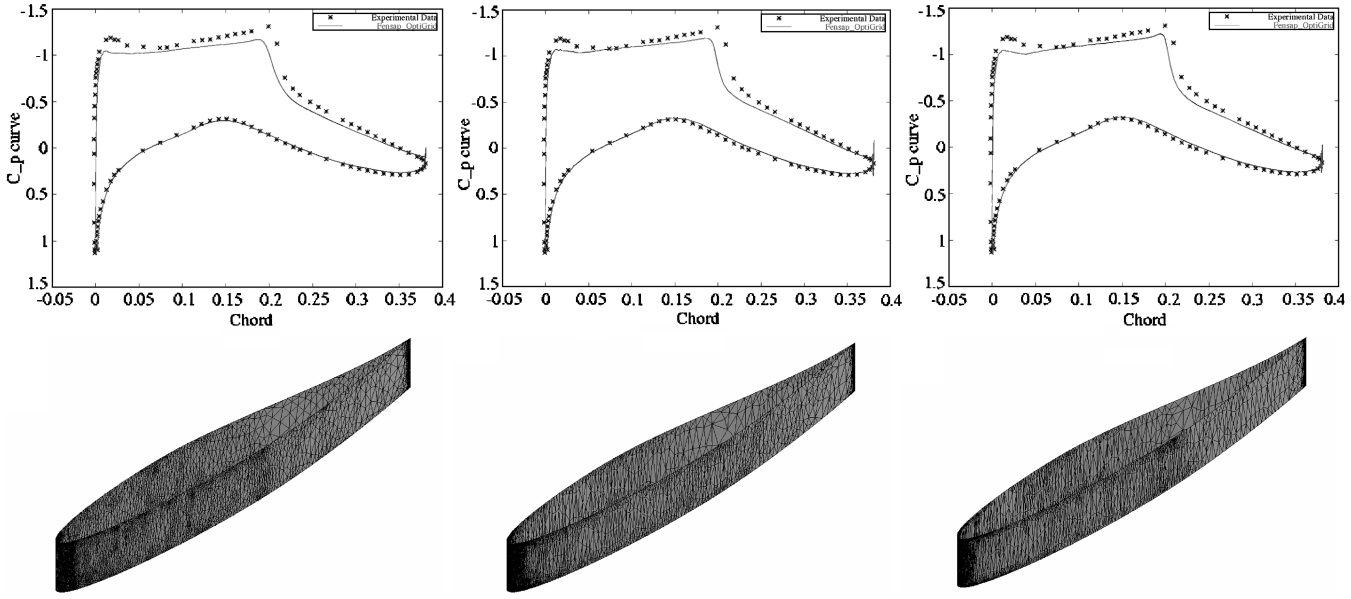

Fig. 12 RAE 2822 wing: Cp chordwise profiles and adapted grids using HBA. Only cycles 2, 4, and 6 are illustrated.

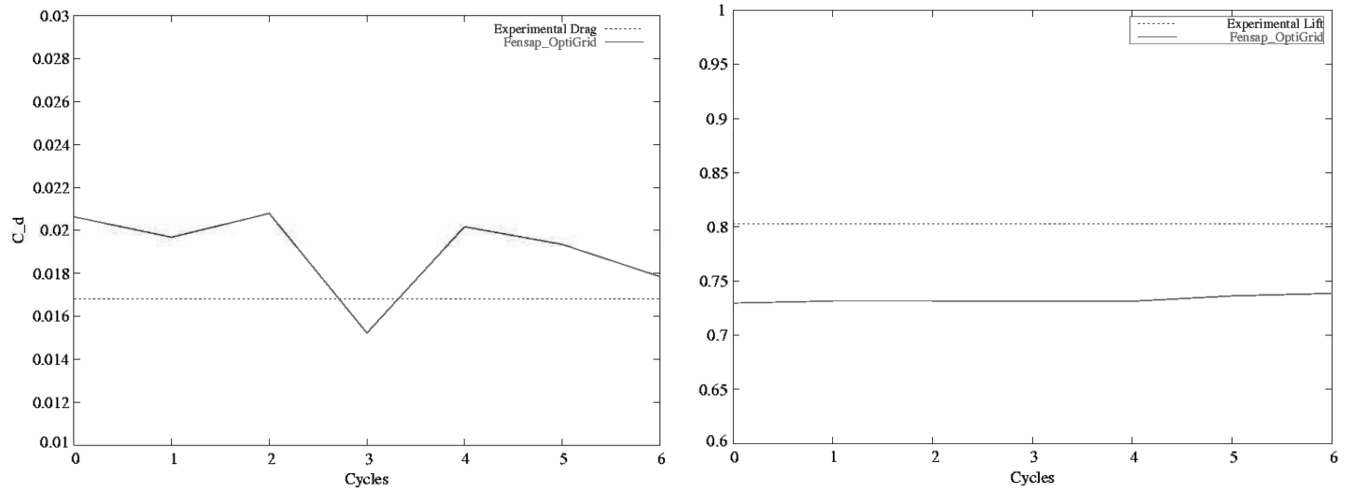

Fig. 13 RAE 2822 wing: drag and lift evolution with adaptation cycles (HBA).

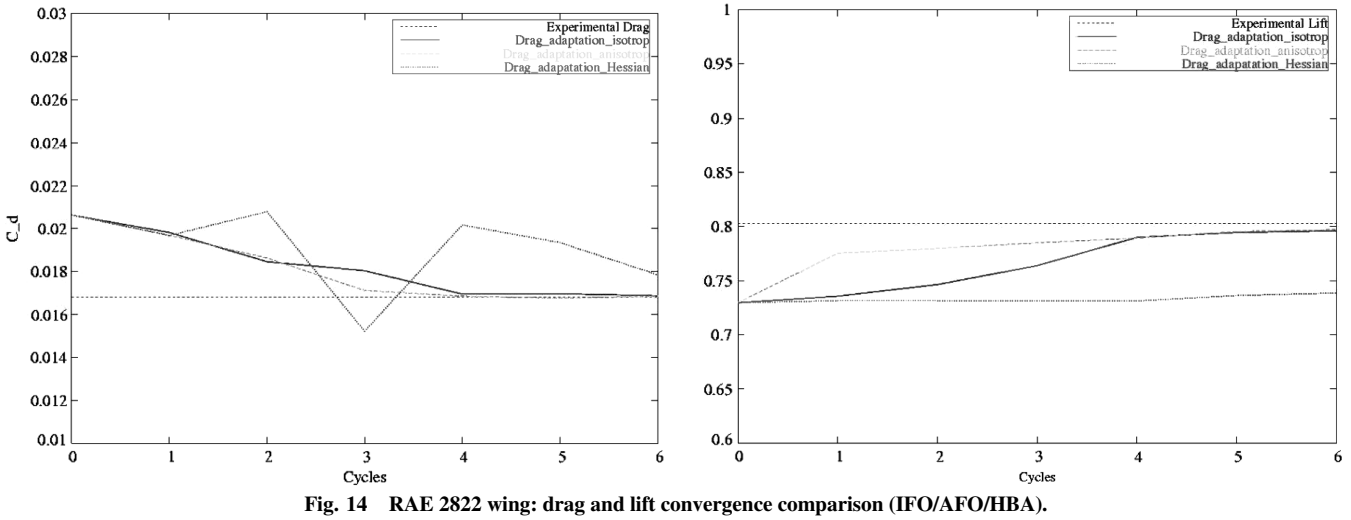

Fig. 14 RAE 2822 wing: drag and lift convergence comparison (IFO/AFO/HBA).

where

$$\begin{pmatrix} y_1 \\ y_2 \\ y_3 \end{pmatrix} = R^t X$$

The volume of the ellipsoid is given by

$$V = \frac{4}{3}\pi \frac{1}{\sqrt{\lambda_1}} \times \frac{1}{\sqrt{\lambda_2}} \times \frac{1}{\sqrt{\lambda_3}}$$

Assuming that $\lambda_1 \geq \lambda_2 \geq \lambda_3$, define the two stretching coefficients by

$$R_1 = \frac{\sqrt{\lambda_2}}{\sqrt{\lambda_1}}, \qquad R_2 = \frac{\sqrt{\lambda_3}}{\sqrt{\lambda_2}}$$

Then, the eigenvalues could be expressed in terms of V, R_1, and R_2 as follows:

$$\lambda_1 = \left(\frac{5\pi}{4R_1^2 R_2 V}\right)^{2/3}, \qquad \lambda_2 = \left(\frac{5\pi R_1}{4R_2 V}\right)^{2/3}$$

$$\lambda_3 = \left(\frac{5\pi R_1 R_2^2}{4V}\right)^{2/3}$$

Now, let E_i be the integration error derived in Sec. II. The transformation in the case of isotropic adaptation transforms a sphere into another sphere with a different radius and volume given by

$$V_{E_i} = \tfrac{4}{3}\pi(1/E_i)^{3/2}$$

To perform an anisotropic functional-output-based mesh adaptation, the volume V in the eigenvalue expression is replaced by V_{E_i} and then the new metric is built. Note that using this expression of the eigenvalues allows the control of the mesh stretching, if desired, through the values of R_1 and R_2.

VI. Numerical Results

To demonstrate the efficiency of the proposed functional-output-based mesh adaptation strategy, the RAE 2822 wing is selected as test case with the drag considered as the functional output and the pressure selected as the variable for integral-error estimation for both drag and lift. This may not be an optimal choice, and more appropriate and specific scalars could be considered for optimal results. Finally, the Mach number is selected to compute the Hessian-based metric.

The flow is simulated using the Spalart–Allmaras turbulence model, under the flight conditions and reference dimensions summarized in Table 1. The proposed isotropic (IFO) and anisotropic (AFO) functional output-based mesh adaptation, as well as the Hessian-based (HBA) mesh adaptation, are applied and compared. Six cycles of adaptation are performed.

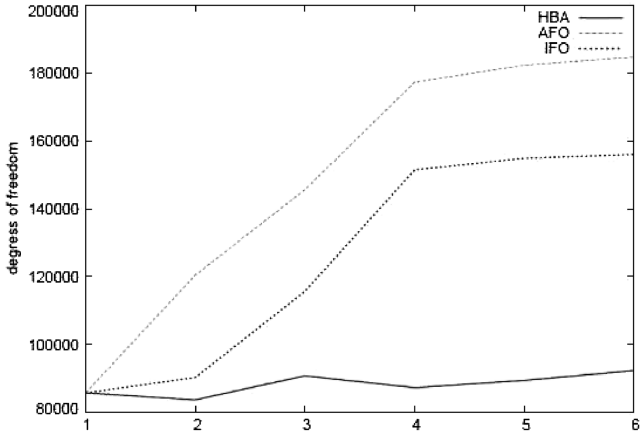

Fig. 15 RAE 2822 wing: evolution of degrees of freedom with cycles of adaptation.

Table 3 ONERA M6 wing test case reference data

Mach number	0.8395
Reynolds number	11.72×10^6
Angle of attack, deg	3.06
Angle of sideslip, deg	0.0
Freestream static pressure, Pa	93.993
Freestream static temperature, K	288

Figures 3–9 show good agreement between the present numerical solution and the experimental results [16] for the case of functional output mesh adaptation. Moreover, an asymptotic convergence of the drag and lift to the experimental values is obtained. The convergence is accelerated when the AFO is used. This allows gaining one cycle of adaptation over four (25% effort saved), because after four cycles no significant changes are observed.

Figure 10 shows a comparison between adapted grids with anisotropic and isotropic methods for the sixth cycle. However, as expected, the Hessian-based method does not give satisfactory results, as shown in Figs. 11–14, unless additional cycles of adaptation are performed. It is clear that, for shock capturing and total node number reduction, the anisotropic approach is preferable, as long, of course, as the limit of the solver in terms of supporting the

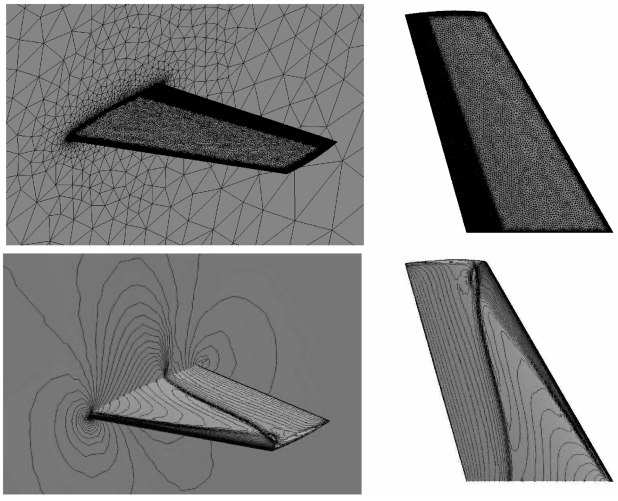

Fig. 16 ONERA M6 wing: initial grid and Cp solution.

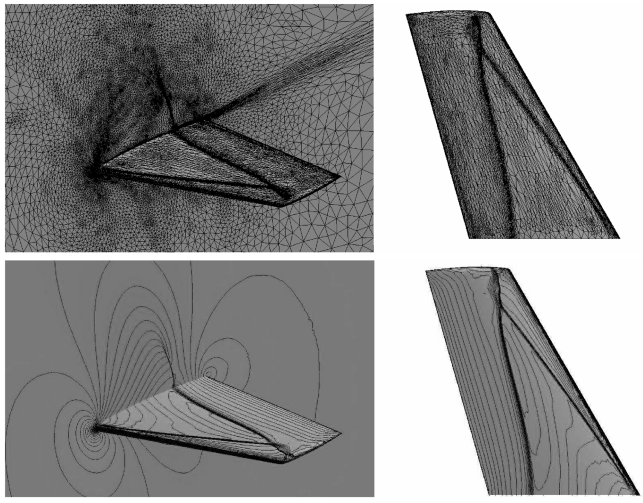

Fig. 17 ONERA M6 wing: grid and Cp solution after five cycles of adaptation using AFO.

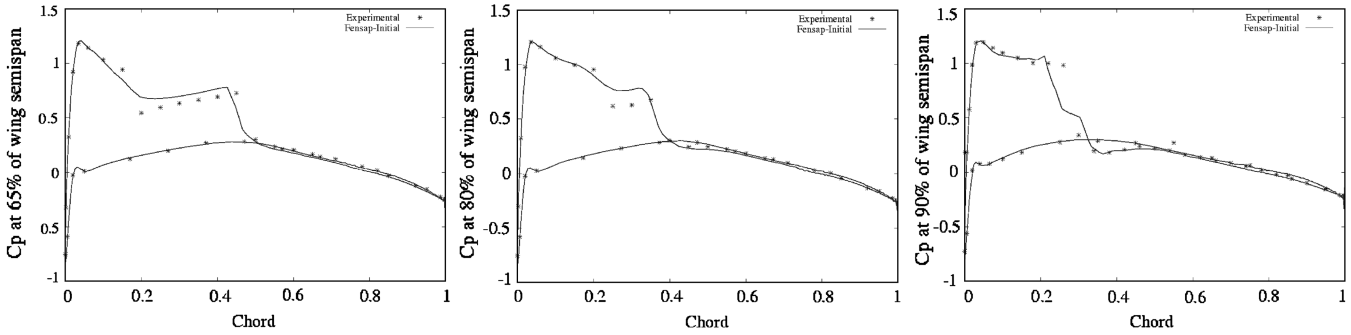

Fig. 18 ONERA M6 wing: Cp chordwise profile on the initial grid.

stretched meshes is not reached, a problem mostly with finite volume solvers. Table 2 compares the drag and lift values for the three methods and the experiment and results from Tezduyar et al. [17]. For a fairer comparison, a curve of degrees of freedom versus cycles of adaptation is shown in Fig. 15. One can indeed see that the number of nodes for the case with the HBA method is less than the number of nodes in the cases with the other methods, but unfortunately this is not the main reason for the poor results shown by this approach. This is more related to the nodes distribution, precisely, the sudden growth of element sizes. Moreover, note that the procedure is fully automatic

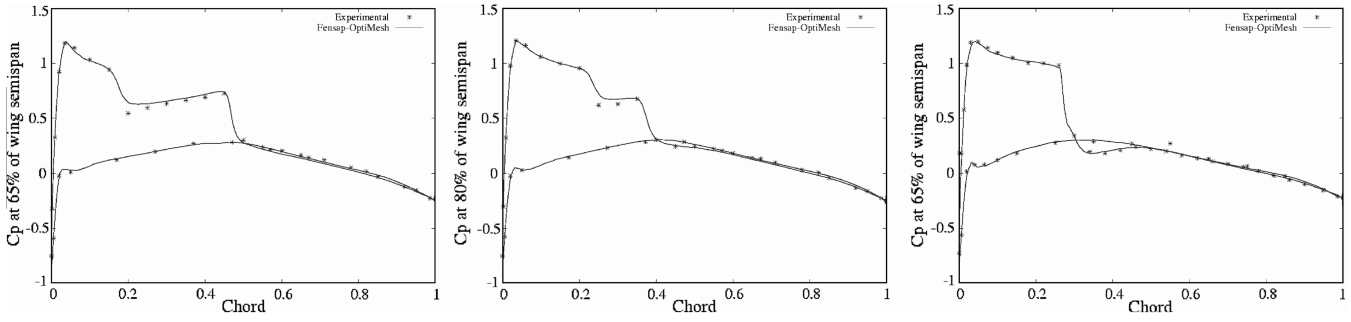

Fig. 19 ONERA M6 wing: Cp chordwise profile after five cycles of adaptation (AFO).

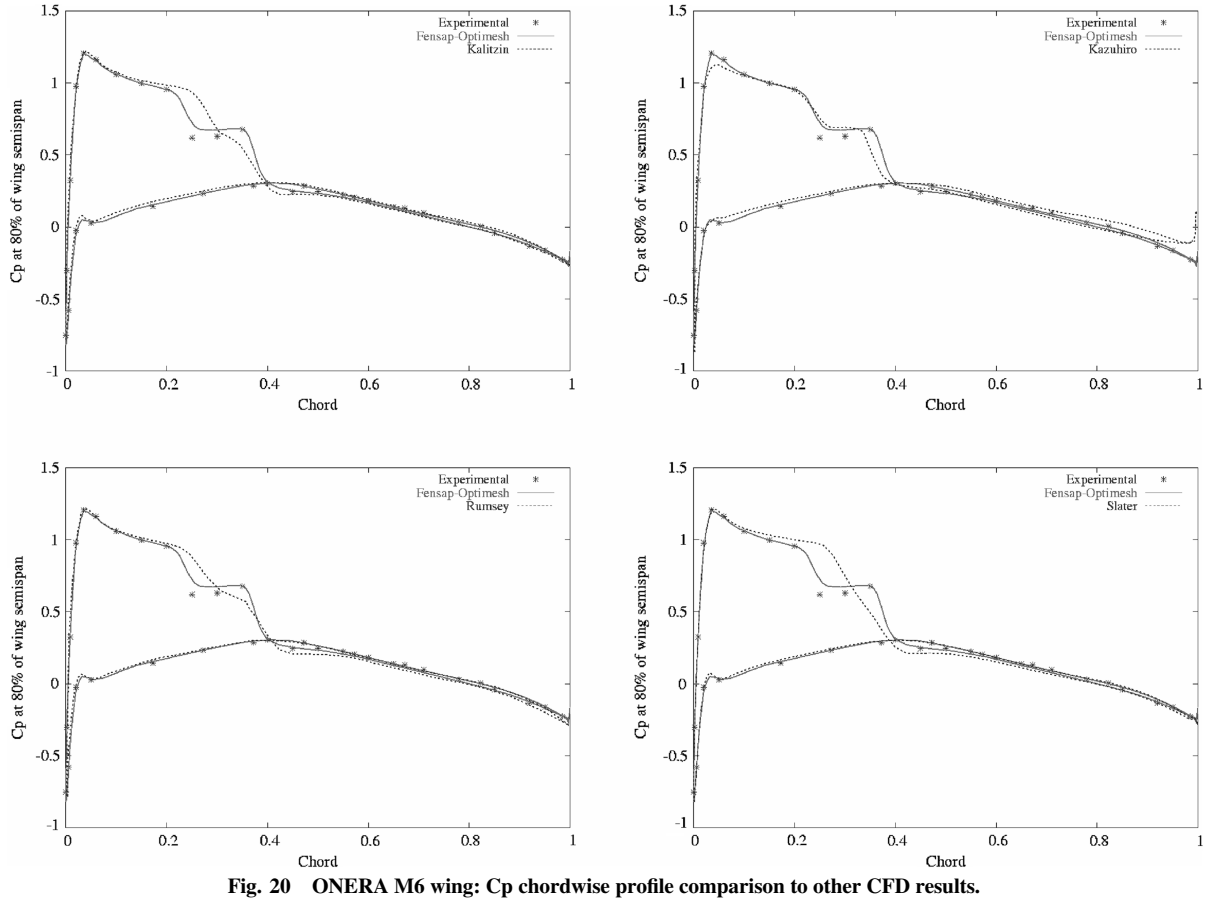

Fig. 20 ONERA M6 wing: Cp chordwise profile comparison to other CFD results.

for all methods, no number of nodes is specified in any case, and the very slow node number increase with adaptation shown in the figure demonstrates that a considerable number of cycles are needed to achieve a noticeable change in the solution.

To show that the functional output strategy not only improves the global values of drag and lift but also the flowfield accuracy, an ONERA M6 wing is selected. It is well known that, for a turbulent transonic flow, the lambda shock is not easy to capture correctly. A viscous flow around this wing was then simulated using the Spalart–Allmaras turbulence model, under the flight conditions and reference dimensions summarized in Table 3. The proposed AFO mesh adaptation approach was applied, and five cycles of adaptation were performed. The C_p curve results are compared with the experiment as well as with a number of other CFD solutions. Figures 16–19 show the C_p solution on the initial grid and on the adapted grid at the 65, 80, and 90% semispan wing sections. A good agreement with experimental results is obtained. Moreover, a comparison with the numerical results presented in [16,18–20], shown in Fig. 20, confirms the superiority of the method and demonstrates its efficiency. The 80% semispan wing section is selected because it is difficult to crisply capture the two shocks close to their intersection point.

VII. Conclusions

In this work, we developed a method based on Hermitian interpolation to estimate an error integral of output quantities such as the drag and lift coefficients. We also proposed a way to achieve anisotropic mesh adaptation in three dimensions by extending the work of Venditti and Darmofal [9,10]. An ISOD stabilized finite element solver is used to solve the Navier–Stokes equations in the turbulent regime. To demonstrate the performance of the proposed method, the RAE 2822 and ONERA M6 wing test cases have been calculated for transonic viscous flows. A comparison with experimental and other CFD tests shows very convincing results.

References

[1] Habashi, W. G., Dompierre, J., Bourgault, Y., Fortin, M., and Vallet, M.-G., "Certifiable Computational Fluid Dynamics Through Mesh Optimization," *AIAA Journal*, Vol. 36, No. 5, 1998, pp. 703–711. doi:10.2514/2.458

[2] Habashi, W. G., Dompierre, J., Bourgault, Y., Ait-Ali-Yahia, D., Fortin, M., and Vallet, M.-G., "Anisotropic Mesh Adaptation: Towards User-Independent, Mesh-Independent and Solver-Independent CFD. Part I: General Principles," *International Journal for Numerical Methods in Fluids*, Vol. 32, 2000, pp. 725–744. doi:10.1002/(SICI)1097-0363(20000330)32:6<725::AID-FLD935>3.0.CO;2-4

[3] Remaki, L., Lepage, C. Y., and Habashi, W. G., "Efficient Anisotropic Mesh Adaptation on Weak and Multiple Shocks," AIAA Paper 2004-0084, 2004.

[4] Remaki, L., and Habashi, W. G., "Efficient Anisotropic Mesh Adaptation on Weak and Multiple Shocks," AIAA Paper 2004-0084, 2004.

[5] Lepage, C. Y., Suerich-Gulick, F., and Habashi, W. G., "Anisotropic 3-D Mesh Adaptation on Unstructured Hybrid Meshes," AIAA Paper 2002-0859, 2002.

[6] Pierce, N. A., and Giles, M. B., "Adjoint Recovery of Superconvergent Functionals from PDE Approximations," *SIAM Review*, Vol. 42, No. 2, 2000, pp. 247–264. doi:10.1137/S0036144598349423

[7] Baker, T. J., "Mesh Adaptation Strategies for Problems in Fluid Dynamics," *Finite Elements in Analysis and Design*, Vol. 25, 1997, pp. 243–273. doi:10.1016/S0168-874X(96)00032-7

[8] Larson, M. G., and Barth, T. J., "A Posteriori Error Estimation for Discontinuous Galerkin Approximations of Hyperbolic Systems," National Academy of Sciences Technical Rept. NAS-99-010, 1999.

[9] Venditti, D. A., and Darmofal, D. L., "Adjoint Error Estimation and Grid Adaptation for Functional Outputs: Application to Quasi One-Dimensional Flow," *Journal of Computational Physics*, Vol. 164, 2000, pp. 204–227. doi:10.1006/jcph.2000.6600

[10] Venditti, D. A., Darmofal, D. L., "Anisotropic Grid Adaptation for Functional Outputs: Application to Two-Dimensional Viscous Flows," *Journal of Computational Physics*, Vol. 187, 2003, pp. 22–46. doi:10.1016/S0021-9991(03)00074-3

[11] Becker, R., and Rannacher, R., "An Optimal Control Approach to A Posteriori Error Estimation in Finite Element Methods," *Acta Numerica 2001*, edited by A. Iserles, Cambridge Univ. Press, Cambridge, England, U.K., 2001.

[12] Hartmann, R., and P. Houston, P., "Goal-Oriented A Posteriori Error Estimation for Multiple Target Functionals," *Hyperbolic Problems: Theory, Numerics, Applications*, edited by T. Y. Hou, and E. Tadmor, Springer, New York, 2003, pp. 579–588.

[13] Remaki, L., Beaugendre, H., and Habashi, W. G., "ISOD—An Anisotropic Isovalues-Oriented Diffusion Artificial Viscosity. Formulation and Application to Euler and Navier–Stokes Equations," *Journal of Computational Physics*, Vol. 186, No. 1, 2003, pp. 279–294. doi:10.1016/S0021-9991(03)00066-4

[14] Remaki, L., and Habashi, W. G., "3-D Mesh Adaptation on Multiple Weak Discontinuities and Boundary Layers," *Journal of Scientific Computing*, Vol. 28, No. 4, 2006, pp. 1379–1397. doi:10.1137/S1064827503429879

[15] Fortin, M., and Fortin, A., "Newer and Newer Elements for Incompressible Flow," *Finite Element in Fluids*, Vol. 1, No. 6, 1985, pp. 171–187.

[16] Kalitzin, G., *Application of the v2-f Turbulence Model to Transonic Flows*, Center of Turbulence Research, Stanford Univ., Palo Alto, CA, 2000.

[17] Tezduyar, T. E., Glowinski, R., and Liou, J., "Petrov–Galerkin Methods on Multi-Connected Domains for the Vorticity-Stream Function Formulation of the Incompressible Navier–Stokes Equations," *International Journal for Numerical Methods in Fluids*, Vol. 8, No. 10, 1988, pp. 1269–1290. doi:10.1002/fld.1650081012

[18] Nakahashi, K., Sharov, D., Kano, S., and Kodera, M., "Applications of Unstructured Hybrid Grid Method to High-Reynolds Number Viscous Flows," *International Journal for Numerical Methods in Fluids*, Vol. 31, 1999, pp. 97–111. doi:10.1002/(SICI)1097-0363(19990915)31:1<97::AID-FLD957>3.0.CO;2-D

[19] Rumsey, C. L., and Vasta, V. N., "A Comparison of the Predictive Capability of Several Turbulent Models Using Upwind and Central Difference Computer Codes," AIAA 93-0192, 1993.

[20] Slater, W. J., "Computational Studies Performed for the ONERA M6 Wing Case," NASA John H. Glenn Research Center at Lewis Field, Aug. 2002; also www.grc.nasa.gov/WWW/wind/valid/m6wing/m6wing01/m6wing01.html [retrieved 15 May 2009].

[21] Schmitt, V., and Charpin, F., "Pressure Distributions on the ONERA-M6-Wing at Transonic Mach Numbers," AGARD, Report AR-138, 1979.

K. Powell
Associate Editor